DE GRUYTER

Nanotechnology Reviews 2025; 14: 20250220

Research Article

Essam Awwad* and Ahmed M. Megahed

Enhancing convective heat transfer mechanisms through the rheological analysis of Casson nanofluid flow towards a stagnation point over an electro-magnetized surface

https://doi.org/10.1515/ntrev-2025-0220
received May 26, 2025; accepted August 17, 2025

Abstract: This research explores the enhancement of heat transfer efficiency using nanofluids influenced by magnetic fields and thermal radiation near a stagnation point. The study involves modeling the flow dynamics over a stretched surface to better understand the mechanisms contributing to heat transfer improvement. To achieve this, a model incorporating variable thermal conductivity and the nonlinear Rosseland radiation approximation is developed. Additionally, it incorporates the influence of magnetic fields to provide deeper insight into their combined impact on the heat transfer process. The focus is on nanofluid flow over a stretched surface, a common scenario in industrial and engineering applications such as cooling systems and heat exchangers. The methodology involves transforming the governing partial differential equations into a set of nonlinear ordinary differential equations, which are solved numerically via shooting technique to analyze fluid dynamics and heat transfer characteristics. The study uniquely integrates variable thermal conductivity and nonlinear radiation effects, offering a more comprehensive perspective on nanofluid behavior under combined influences. Key findings reveal that increasing Brownian motion leads to a thicker thermal boundary layer and elevated temperature profiles, aligning with prior research while reinforcing the robustness of the employed numerical approach. These results validate the proposed model and confirm its reliability in predicting nanofluid heat transfer behavior, contributing to the optimization of thermal management systems in industrial applications.

Keywords: nanofluid, stagnation point, numerical solution, Joule heating, Brownian motion, viscous dissipation

Nomenclature

a	positive factor that measures the stretching velocity $(\frac{1}{\mathrm{s}})$
b	positive constant $(\frac{1}{\mathrm{s}})$
B_0	index that quantifies the magnetic field's magnitude (T)
D_B	factor that determines mass transport by diffusion ($\mathrm{m}^2\ \mathrm{s}^{-1}$)
B_i	dimensionless Biot number
h	dimension thermal convection coefficient ($\mathrm{W\ m}^{-2}$)
C_∞	far-field fluid concentration relative to the sheet ($\mathrm{mol\ L}^{-1}\ \mathrm{mol}$)
k^*	mean absorption coefficient (m^{-1})
c_p	heat storage capacity per unit mass ($\mathrm{kg}^{-1}\ \mathrm{K}^{-1}\ \mathrm{J}$)
D_T	measure quantifying the effect of thermophoretic phenomenon ($\mathrm{s}^{-1}\ \mathrm{m}^2$)
C_w	concentration of nanofluid beside the sheet ($\mathrm{L}^{-1}\ \mathrm{mol}$)
Pr	dimensionless Prandtl number
Ec	dimensionless Eckert number
M	factor of magnetic field
C	concentration ($\mathrm{L}^{-1}\ \mathrm{mol}$)
T_f	surface temperature where convection occurs (K)
Le	dimensionless Lewis number
R_d	dimensionless radiation parameter
T_∞	ambient temperature condition (K)

*** Corresponding author: Essam Awwad,** Department of Mathematics, College of Science, Jouf University, Al-Jawf, Saudi Arabia, e-mail: emawwad@ju.edu.sa
Ahmed M. Megahed: Department of Mathematics, Faculty of Science, Benha University, Benha, Egypt, e-mail: ahmed.abdelbaqk@fsc.bu.edu.eg

q_r	radiant energy flow per unit area (W m^{-2})
x, y	perpendicular axis coordinates (m)
uv	directional velocity components (m s^{-1})
Greek symbols	
ν	kinematic viscosity (m^2 s^{-1})
θ	dimensionless temperature
μ	dynamic viscosity (s^{-1} m^{-1} kg)
σ^*	Stefan–Boltzmann constant (W m^{-2} K^{-4})
θ_w	parameter regarding the temperature ratio
η	similarity coefficient
ϕ	dimensionless concentration
δ	dimensionless Casson parameter
ρ	density (m^{-3} kg)
σ_e	conductance per unit length (m^{-1} s)
κ	thermal conductivity (m^{-1} W K^{-1})
Γ_b	stochastic motion parameter
τ	heat capacity proportion between nanoparticles and fluid (mol^{-1} L)
Γ_t	particle migration parameter under thermal gradient
Ω	suction velocity parameter
β	ratio of sheet velocity to free stream velocity

1 Introduction

Nanofluid flow, emerging at the nexus of nanotechnology and fluid mechanics, holds great promise across various sectors, including maritime applications. Nanofluids consist of nanoparticles dispersed within a base fluid [1]. These nanoparticles impart unique and customizable characteristics to nanofluids, significantly improving their performance in various applications. They enhance heat transfer [2], lubrication [2], and electronic cooling [3] and play a crucial role in nuclear energy systems [4] as well as heating and cooling processes [5]. Additionally, they modify the behavior of the fluids [6], making them more versatile and efficient for specific needs. In maritime contexts, where efficient heat exchange, corrosion resistance, and fluid flow optimization are vital, nanofluids offer significant advantages. Utilizing the remarkable thermal conductivity and rheological properties of nanofluids, maritime systems can benefit from better engine cooling, more efficient heat exchangers, and superior machinery lubrication. Additionally, customized nanofluid properties can prevent fouling and corrosion in maritime equipment, thereby extending operational lifespans and lowering maintenance costs. This introduction sets the stage for examining the numerous applications of nanofluid flow in the maritime industry, highlighting its potential to drive innovation and tackle significant challenges in maritime engineering and operations.

Magnetohydrodynamics, often abbreviated as MHD, represents an amalgamation of principles from fluid mechanics and electromagnetism [7]. In essence, it delves into the intricate interactions between magnetic fields and electrically conducting fluids [8]. This interdisciplinary field explores how magnetic fields influence the behavior and dynamics of such fluids, offering insights into phenomena ranging from astrophysical plasma flows to industrial applications like magnetic confinement fusion reactors [9]. Here, we provide a comprehensive overview of numerous recent studies that explore the influence of MHD on various flow and heat transfer phenomena. These investigations delve into the effects of thermal radiation and non-uniform heat sources [10], as well as the generation and absorption of heat [11]. The studies encompass scenarios involving natural convection and the behavior of nanofluids near stagnation points [12], highlighting the significant role of MHD in these processes. Khan *et al.* [13–16] have significantly advanced MHD nanofluid modeling through fractional calculus and complex boundary analyses. Their initial work employed fractional derivatives to study natural convection in Darcy porous media, capturing nonlocal heat transfer effects. Subsequent research integrated distributed fractional-order derivatives for Darcy–Forchheimer porous flows, enhancing modeling precision. A key innovation combined fractional derivatives with the Cattaneo heat flux model to account for finite thermal wave speeds in MHD systems. Most recently, they investigated nanofluid heat transfer over three-dimensional (3D) irregular surfaces with magnetic and slip effects, offering new insights into complex flow regulation. These studies predominantly center on scenarios involving the presence of a magnetic field and the flow behavior of fluids such as liquid metals, water with minor acid additives, and other industrially relevant fluids. Specifically, they delve into understanding the flow and heat transfer characteristics of viscous, incompressible fluids flowing past either a moving plate or a stretching surface.

Recent advances in modeling Casson nanofluids have deepened insights into thermal and mass transport phenomena across diverse physical scenarios. Ganesh and Sridhar [17] analyzed MHD Casson nanofluid flow with chemical reactions and porous media resistance (Darcy–Forchheimer model), uncovering how these factors modify heat transfer dynamics. Singh *et al.* [18] analyzed MHD flow of a Casson fluid with combined Navier and second-order slip effects past a permeable stretching/shrinking surface. Jaffrullah *et al.* [19] expanded on this by integrating

Joule heating, demonstrating its influence on thermal profiles in porous systems. Employing spectral methods, Awati *et al.* [20] performed stability studies on MHD Casson fluid dynamics near exponentially contracting boundaries. Lone *et al.* [21] extended the framework by incorporating bioconvection in stratified Casson flows with microorganisms and activation energy impacts. Rani *et al.* [22] studied hybrid nanofluids near stagnation regions, revealing improved thermal efficiency due to synergistic nanoparticle interactions. Additionally, Jaffrullah *et al.* [23] explored suction, radiation, and nonlinear stretching effects, providing deeper insights into flow control for industrial applications. Further advancing the field, Nihaal *et al.* [24] developed a stochastic approach to investigate bioconvective Casson nanofluid transport with chemical reactions past slender needle geometries. Further, the study of nanofluid flow in conjunction with thermal radiation and magnetic fields has been explored through various models. One such model is the Casson nanofluid model, which is detailed in the study of Elham Alali and Megahed [25]. Another approach involves Newtonian nanofluids under conditions of prescribed heat flux and viscous dissipation, as described in the study of Ghoneim and Megahed [26]. Additionally, the tangent hyperbolic nanofluid model addresses the impact of slip phenomena, as outlined in the study of Amer *et al.* [27]. This area of research is crucial for several reasons: it enhances our understanding of heat transfer efficiency, elucidates the combined effects of different physical forces, drives technological advancements, provides insights into complex multi-physics phenomena, offers solutions to environmental and energy-related challenges, and opens up new avenues for scientific investigation. This cross-disciplinary method holds promise for discovering innovative approaches to effective thermal control and promoting sustainable technological progress.

This study utilizes the shooting method to numerically analyze the behavior of Casson nanofluid flow, heat transfer, and nanoparticle dispersion near a stretching surface close to a stagnation point. It addresses a research gap by examining the combined effects of variable thermal conductivity, nonlinear Rosseland radiation, thermophoresis, Brownian motion, thermal radiation, viscous dissipation, and magnetic fields on heat and mass transfer. The work distinguishes itself by integrating these factors to improve predictive accuracy. The results have practical implications for industrial cooling, heat exchangers, and thermal management technologies. The Casson nanofluid is chosen for its superior thermal conductivity and stability, making it ideal for applications requiring efficient heat dissipation in engineering and manufacturing. This study has broad practical implications, particularly in metallurgy and polymer technology. Potential applications include optimizing ship engine cooling via marine propulsion systems, boosting performance in industrial and maritime heat exchangers, refining cooling methods for vessels, improving temperature regulation in chemical processing, advancing solar thermal collector efficiency, and enhancing precision in thermal therapies.

2 Mathematical model

As illustrated in this section, we analyze a two-dimensional steady boundary layer flow of a Casson nanofluid influenced by thermal radiation and induced by flow over a stretching sheet. The stretching sheet is characterized by a linear velocity profile of $u_w = ax$, where a represents a constant value (Figure 1):

By incorporating this model, an analysis of heat transfer is conducted in the presence of viscous dissipation, Joule heating, and thermal radiation properties. In this case, we consider that a perpendicular to the flow direction homogeneous magnetic field of intensity B_0 is applied. Joule heating plays a key role in nanofluid flow because it modifies fluid dynamics, improves thermal management, increases heat transfer, affects temperature distribution, and increases energy efficiency. In the subsequent set of governing equations, we make the assumption that T_f denotes the temperature at the convective surface, T_w represents the temperature of the sheet, and T_∞ represents the temperature of the surrounding ambient fluid. In the current model, the flow takes place adjacent to an incompressible stagnation point, a feature of significant importance in various applicable fields. For this nanofluid, the incompressible stagnation-point flow can

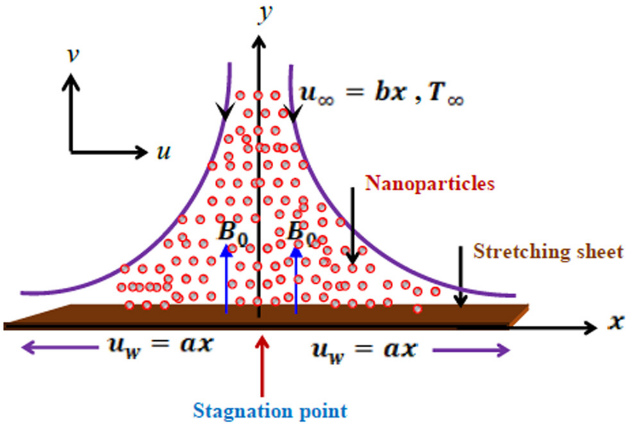

Figure 1: The flow configuration and coordinate system.

therefore be described by the following two-dimensional stable boundary layer equations [28]:

$$\frac{\partial u}{\partial x} + \frac{\partial v}{\partial y} = 0, \tag{1}$$

$$\begin{aligned} u\frac{\partial u}{\partial x} + v\frac{\partial u}{\partial y} &= \frac{\mu}{\rho}\left(1 + \frac{1}{\delta}\right)\frac{\partial^2 u}{\partial y^2} + u_\infty \frac{du_\infty}{\partial x} \\ &\quad - \frac{\sigma_e B_0^2}{\rho}(u - u_\infty), \end{aligned} \tag{2}$$

$$\begin{aligned} u\frac{\partial T}{\partial x} + v\frac{\partial T}{\partial y} &= \frac{\kappa}{\rho c_p}\left(\frac{\partial^2 T}{\partial y^2}\right) + \frac{\sigma_e B_0^2}{\rho c_p}(u_\infty - u)^2 \\ &\quad + \frac{\mu}{\rho c_p}\left(1 + \frac{1}{\delta}\right)\left(\frac{\partial u}{\partial y}\right)^2 \\ &\quad + \tau\left\{D_B \frac{\partial C}{\partial y}\frac{\partial T}{\partial y} + \frac{D_T}{T_\infty}\left(\frac{\partial T}{\partial y}\right)^2\right\} - \frac{1}{\rho c_p}\frac{\partial q_r}{\partial y}, \end{aligned} \tag{3}$$

$$u\frac{\partial C}{\partial x} + v\frac{\partial C}{\partial y} = \frac{D_T}{T_\infty}\frac{\partial^2 T}{\partial y^2} + D_B \frac{\partial^2 C}{\partial y^2}. \tag{4}$$

The boundary conditions outlined for the problem under consideration are as follows:

$$\begin{aligned} &u = u_w(x) = ax, \quad v = -v_w \quad -\kappa\frac{\partial T}{\partial y} = h(T - T_f), \\ &C = C_w \quad \text{at } y = 0, \end{aligned} \tag{5}$$

$$u \to u_\infty(x) = \mathrm{b}x, \quad T \to T_\infty, \quad C \to C_\infty \quad \text{as } y \quad \to \infty. \tag{6}$$

Here, we must mention that the convective heat transfer condition is vital because it accurately models the heat exchange between the nanofluid and its environment, a key factor in applications such as cooling systems and heat exchangers. Incorporating this condition enhances the model's practicality by capturing the interplay between internal conduction and external convection, improving the understanding of heat dissipation. As evident from the earlier system, which governs our physical model through equations (1) to (4), the behavior of the model under physical phenomena is characterized by nonlinear partial differential equations (PDEs). Now, by employing the Rosseland approximation to characterize thermal radiation and applying it to materials with high optical density, the radiative heat flux can be calculated, as described in the works of Raptis [29], Brewster [30], and Sparrow and Cess [31]:

$$q_r = -\frac{16\sigma^*}{3k^*}\left(T^3 \frac{\partial T}{\partial y}\right). \tag{7}$$

Here, σ^* denotes the Stefan–Boltzmann constant and k^* signifies the mean absorption coefficient. Therefore, equation (3) can be expressed as

$$\begin{aligned} &u\frac{\partial T}{\partial x} + v\frac{\partial T}{\partial y} \\ &\quad = \frac{\partial}{\partial y}\left[\left(\kappa + \frac{16\sigma^* T^3}{3\rho c_p k^*}\right)\frac{\partial T}{\partial y}\right] \\ &\qquad + \frac{\sigma_e B_0^2}{\rho c_p}(u_\infty - u)^2 + \frac{\mu}{\rho c_p}\left(1 + \frac{1}{\delta}\right)\left(\frac{\partial u}{\partial y}\right)^2 \\ &\qquad + \tau\left\{D_B \frac{\partial C}{\partial y}\frac{\partial T}{\partial y} + \frac{D_T}{T_\infty}\left(\frac{\partial T}{\partial y}\right)^2\right\} \\ &\qquad - \frac{1}{\rho c_p}\frac{\partial q_r}{\partial y}. \end{aligned} \tag{8}$$

By implementing dimensionless variables in the specified format [27]:

$$\eta = \sqrt{\frac{a}{\nu}}y, \quad u = axf'(\eta), \quad \phi(\eta) = \left(\frac{C - C_\infty}{C_w - C_\infty}\right), \tag{9}$$

$$v = -\sqrt{a\nu}f(\eta), \quad \theta(\eta) = \left(\frac{T - T_\infty}{T_w - T_\infty}\right). \tag{10}$$

The similarity variable η is introduced through carefully selected transformations to convert the governing PDEs into a system of ODEs, leveraging the self-similar characteristics inherent to stagnation-point flows. The velocity components u and v, along with the dimensionless functions θ and ϕ, are defined to achieve appropriate scaling while maintaining analytical tractability within boundary layer theory. Therefore, equations (2) through (4) undergo a conversion procedure that converts them into a non-dimensional ordinary differential equation format, using the similarity transformation given in equations (9) through (10). The steps involved in this conversion procedure are as follows:

$$\left(1 + \frac{1}{\delta}\right)f''' - f'^2 + ff'' + \beta^2 + M(\beta - f') = 0, \tag{11}$$

$$\begin{aligned} &\frac{1}{\mathrm{Pr}}(\theta''\{1 + R_d[\theta(\theta_w - 1) + 1]^3\}) + \frac{3R_d}{\mathrm{Pr}} \\ &\quad \times (\theta'^2(\theta_w - 1)[\theta(\theta_w - 1) + 1]^2) + f\theta' + \Gamma_t\theta'^2 \\ &\quad + \Gamma_b\phi'\theta' + \mathrm{Ec}\left(1 + \frac{1}{\delta}\right)f''^2 + M\mathrm{Ec}(\beta - f')^2 = 0, \end{aligned} \tag{12}$$

$$\phi'' + Lef\phi' + \frac{\Gamma_t}{\Gamma_b}\theta'' = 0. \tag{13}$$

In this context, it is important to highlight that the preceding system of equations (11) through (13) is exceedingly nonlinear and cannot be resolved through analytical means alone. Consequently, the utilization of numerical techniques becomes imperative to tackle the complexity inherent in the system.

Additionally, the associated boundary conditions for our specific problem are expressed as follows:

$$\begin{gathered} f(\eta) = \Omega, \quad f'(\eta) = 1, \quad \phi(\eta) = 1, \\ \theta'(\eta) = -B_i(1 - \theta(\eta)) \text{ at } \eta = 0, \end{gathered} \tag{14}$$

$$f'(\eta) \to \beta, \quad \theta(\eta) \to 0, \quad \phi(\eta) \to 0 \quad \text{as } \eta \to \infty, \tag{15}$$

where B_i is the Biot number, Ω is the suction velocity, β is the proportion between the stretched sheet's velocity and the rates of free stream velocity, M is magnetic parameter, Pr is the Prandtl number, R_d is the radiation parameter, and Ec is the Eckert number, Γ_t is the thermophoresis parameter and Γ_b is the Brownian motion parameter. These factors defined below as

$$\begin{gathered} B_i = \frac{h}{\kappa\sqrt{\frac{\rho c_p \nu}{\kappa}}}, \quad \Omega = \frac{v_w}{\sqrt{a\nu}}, \quad M = \frac{\sigma B_0^2}{\rho a}, \\ \Pr = \frac{\rho c_p \nu}{\kappa}, \quad \Gamma_b = \tau D_B(C_w - C_\infty)/\nu, \end{gathered} \tag{16}$$

$$\begin{gathered} R_d = 16\sigma^* T_\infty^3/3\kappa k^*, \beta = \frac{a}{b}, \mathrm{Ec} = u_w^2/c_p(T_f - T_\infty), \\ \Gamma_t = \tau D_T(T_f - T_\infty)/T_\infty \nu. \end{gathered} \tag{17}$$

2.1 Quantities of practical interest

Important features of fluid flow, heat transmission, and mass transfer are measured by the skin friction coefficient, Nusselt number, and Sherwood number. Enhancing mass transfer in chemical and biological processes, reducing drag in fluid dynamics, and improving heat transfer in thermal systems are just a few examples of the many technical and industrial processes that depend on their comprehension and control. The skin friction coefficient, surface heat flux, and mass fluxes can be determined using the specified equations:

$$\begin{gathered} \mathrm{Cf}_x \mathrm{Re}_x^{\frac{1}{2}} = -\left(1 + \frac{1}{\delta}\right) f''(0), \quad \frac{\mathrm{Nu}_x}{\sqrt{\mathrm{Re}_x}} = -(1 + R_d\theta_w^3)\theta'(0), \\ \frac{\mathrm{Sh}_x}{\sqrt{\mathrm{Re}_x}} = -\phi'(0), \end{gathered} \tag{18}$$

where Re_x is the local Reynolds number.

2.2 Limitations of the study

Despite the comprehensive analysis in this study, certain limitations should be noted. First, the mathematical model relies on specific assumptions, such as steady-state, laminar flow, and a uniformly stretched surface, which may not fully capture real-world complexities like turbulence or surface roughness. Additionally, the nanofluid properties were assumed constant, whereas in practical applications, variations in nanoparticle concentration and temperature-dependent thermal conductivity could impact the results. Further, the study uses the Rosseland approximation for thermal radiation, best suited for optically thick media, which may limit its relevance across all nanofluid conditions. Additionally, external forces like gravity and shear-induced diffusion are neglected, potentially affecting heat and mass transfer in specific applications. Future work must aim to diminish these assumptions to enhance the model's relevance for more complex and possible practical engineering situations.

3 Solution methodology

The research examined numerically the magnetohydrodynamic nanofluid stagnation point flow problem with thermal radiation and convective boundary condition by first converting the governing PDEs into dimensionless form through similarity transformations. These transformations yielded coupled nonlinear ODEs for momentum (11), energy (12), and nanoparticle transport (13), which were solved numerically using a shooting technique that coupled with fourth-order Runge–Kutta integration. Initial conditions were iteratively refined via Newton–Raphson until boundary conditions (14) and (15) were satisfied within a 10^{-6} tolerance threshold. Solution accuracy was ensured by implementing the Runge–Kutta scheme with decreasing step increments ($\Delta\eta$ = 0.1, 0.05, 0.025) and comparing results at designated control locations (η = 6.0).

4 Confirmation of the code's precision

In this section, to validate the methodology employed via the shooting method and demonstrate its precision, the results obtained were juxtaposed with those from a prior study conducted by Ghasemi and Hatami [32] for different values of Brownian parameter Γ_b. This comparison was facilitated through Table 1, where the numerical solutions were evaluated against the findings presented in their publication. This table provides numerical data for the reduced Nusselt number calculated using equation (12), along with the corresponding results reported by Ghasemi and Hatami [32]. The close agreement between the values obtained in the current study and those previously reported underscores the excellent concurrence between the two sets of results.

5 Discussion

First, we must mention here that the accurate modeling of nanofluid thermal dynamics near stagnation regions requires simultaneous incorporation of multiple physical effects such as applied magnetic fields, nonlinear radiative transfer, convective heating, and viscous energy dissipation. These coupled phenomena collectively govern velocity and temperature distributions, critically affecting both thermal boundary layer formation and system-wide heat transfer performance in practical applications. As previously stated, the equations that govern the flow of Casson nanofluid over a stretching sheet adjacent to a stagnation point, considering the presence of a magnetic field, thermal radiation, and viscous dissipation, along with their respective boundary conditions, are solved numerically using the shooting method. Within this framework, it is critical to emphasize that the parameter values adopted in this investigation adhere to well-defined bounds. These ranges were meticulously selected to faithfully represent the physical phenomena being studied. The choices were informed by a combination of experimental data and theoretical principles, ensuring consistency with accepted theoretical models while preserving practical applicability. Further, the range of parameters are introduced as $0.0 \le M \le 3.0$, $0.2 \le \beta \le 1.5$, $0.1 \le B_i \le 1.2$, $0.5 \le \theta_w \le 2.5$, $0.0 \le R_d \le 2.5$, $0.0 \le \Gamma_t \le 0.8$, and $0.1 \le \Gamma_b \le 1.8$. Keeping all other governing factors constant, Figure 2 shows how changes in the Casson parameter δ affect the temperature $\theta(\eta)$, velocity $f'(\eta)$, and concentration $\phi(\eta)$ distributions. According to the figures, concentration levels and the Casson parameter have a positive association, with an upsurge in the former resulting in a somewhat higher concentration. On the contrary, the distributions of temperature and velocity show an inverse connection with the Casson parameter, indicating that temperature and velocity tend to drop as the Casson parameter increases. Physically, the reduction in nanofluid temperature with a higher Casson parameter is mainly because of greater flow resistance (higher yield stress), diminished convective heat transfer, increased effective viscosity, a thicker thermal boundary layer, and changes in nanoparticle behavior. These factors together impair the nanofluid's capacity to transport and distribute heat, resulting in a lower overall temperature.

Table 1: Comparison of $-\theta'(0)$ with some values of Brownian parameter Γ_b when $\Pr = 10$, $\Gamma_t = 0.1$, $R_d = Ec = M = \beta = 0$, $B_i \to \infty$, and $\delta \to \infty$

Γ_b	Ghasemi and Hatami [32]	Present work
0.1	0.9528	0.95271043
0.2	0.5057	0.50565809
0.3	0.2527	0.25269002
0.4	0.1196	0.11957890
0.5	0.0546	0.05455786

In order to demonstrate how variations in magnetic intensity impact these parameters, Figure 2 displays the velocity, concentration, and temperature profiles throughout a range of magnetic parameter M values, from 0 to 3. A slight elevation in nanoparticle concentration $\phi(\eta)$ is noted, attributed to the response elicited by the presence of the magnetic field. Furthermore, a markedly elevated temperature distribution $\theta(\eta)$ is observed in the magnetic field; this is because the magnetic field induces more energy transfer mechanisms in the system, which results in increased thermal effects. Moreover, a considerable reduction in the velocity distribution $f'(\eta)$ is observed when the magnetic field is present. Physically, this happens because the magnetic field exerts forces on the fluid that counter its flow direction, causing a drag effect that slows the fluid's movement, leading to a significant reduction in velocity across the system (Figure 3).

The impacts of the velocity ratio parameter β on the thermal characteristics, concentration behavior, and momentum dynamics in nanofluid flow are shown in Figure 4. This figure suggests that combining the velocity ratio parameter's effects can assist mitigate the gradient of temperature distribution and the rate drop in nanoparticle concentration. On the contrary, the velocity distribution shows a different trend when the same parameter is applied. Physically, the reduction in nanofluid concentration as the velocity ratio parameter increases is mainly caused by stronger shear forces, higher turbulence, changes in Brownian motion and dispersion dynamics, centrifugal forces in rotating systems, and variations in boundary layer behavior. Together, these effects result in a more uneven distribution and greater settling of nanoparticles, lowering their concentration in the fluid.

Figure 5 presents the impact of the Biot number B_i on the concentration and temperature profiles of Casson nanofluid flow passing over a stretching sheet. The graph below illustrates how concentration and temperature rise in proportion to increasing Biot number values. The temperature increases substantially, while the concentration just slightly rises. This is explained by the fact that the Biot number directly affects the temperature field, which in turn has an indirect effect on the concentration field. From a thermal

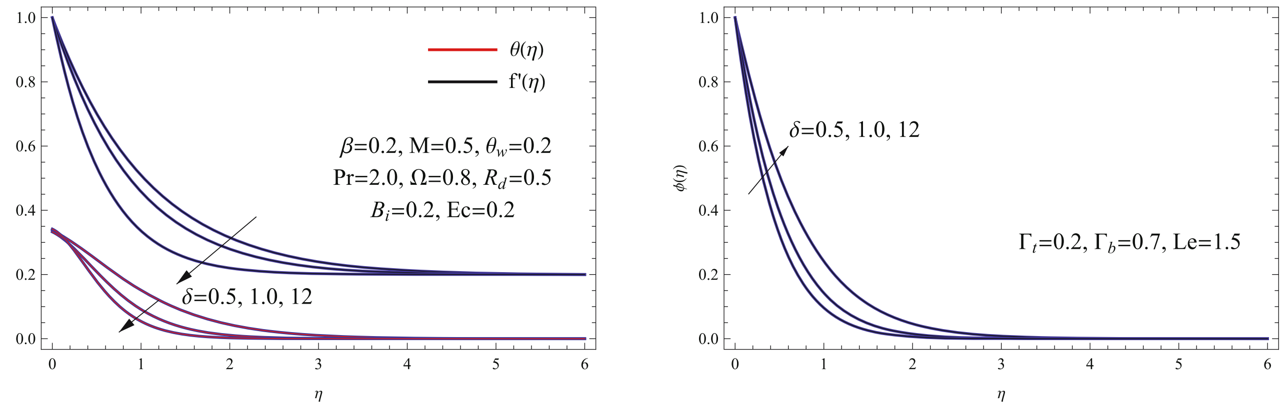

(a) (b)

Figure 2: (a) $f'(\eta)$ and $\theta(\eta)$ for various δ and (b) $\phi(\eta)$ for various δ.

physics perspective, elevated Biot numbers indicate enhanced convective heat transfer at the sheet surface. This augmentation in convective heating generates steeper thermal gradients across the sheet, consistent with established empirical observations. The amplified heat transfer promotes greater thermal diffusion into the adjacent quiescent fluid, consequently expanding both the temperature distribution and thermal boundary layer thickness with increasing Biot number.

Figure 6 illustrates how the temperature profiles are influenced by the temperature ratio parameter θ_w and thermal radiation parameter R_d, considering specific chosen values. At larger values of the temperature ratio parameter, the change in dimensionless temperature shows a more noticeable increase. The thermal radiation parameter shows a similar tendency, especially when it comes to the area farthest from the sheet. Furthermore, it is clear that the effect of thermal radiation away from the sheet returns along the sheet in the presence of the Biot number. Physically, this behavior occurs because changes in the value of Biot number can alter the thickness of the thermal boundary layer, thereby impacting the mechanism of heat transfer away from the surface. By controlling boundary convection effectiveness, the Biot number determines thermal conduction performance into the fluid domain, making overall thermal transport highly sensitive to its value.

Figure 7 illustrates how variations in the thermophoresis parameter Γ_t impact both the thermal field $\theta(\eta)$ and the concentration of nanoparticles $\phi(\eta)$. Initially, it is important to note that the thermophoresis parameter characterizes the extent to which nanoparticles exhibit movement in reaction to temperature differentials within a fluid environment. Elevating the thermophoresis parameter causes a surge in the heat field and the concentration of nanoparticles, as the figure illustrates. Physically and from a transport phenomena viewpoint, enhanced

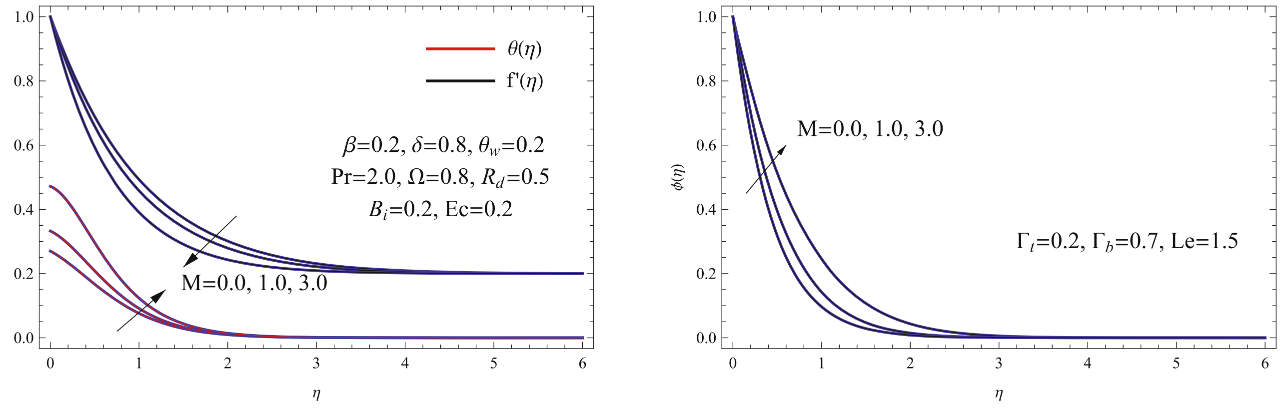

(a) (b)

Figure 3: (a) $f'(\eta)$ and $\theta(\eta)$ for various M and (b) $\phi(\eta)$ for various M.

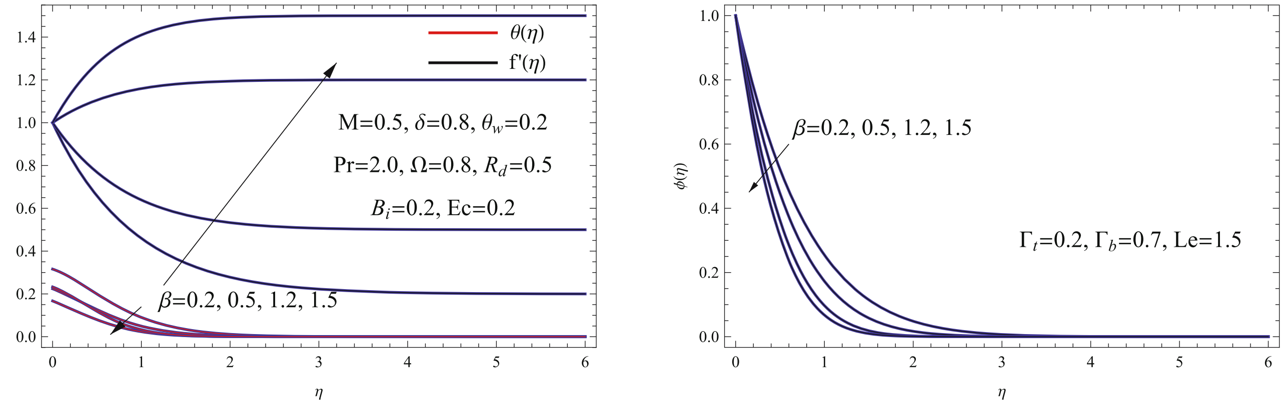

(a) (b)

Figure 4: (a) $f'(\eta)$ and $\theta(\eta)$ for various β and (b) $\phi(\eta)$ for various β.

thermophoretic forces propel nanoparticles toward elevated-temperature zones. Such directional migration produces more homogeneous nanoparticle dispersion with increased local concentrations, which subsequently optimizes heat transfer pathways. This optimization boosts both the intensity and reactivity of the thermal environment.

Figure 8 displays the effects of the chosen parameters' Brownian motion parameter Γ_b on the temperature $\theta(\eta)$ and concentration $\phi(\eta)$ curves. When Brownian motion becomes more significant, the volume percentage of nanoparticles decreases, but the thermal thickness and temperature of the nanofluid increase considerably. This indicates that the difference between temperature distribution and concentration variation is mainly due to the dominant influence of Brownian motion on the dispersion of nanoparticles. This leads to greater fluctuations in temperature distribution compared to changes in nanoparticle concentration because Brownian motion enhances thermal mixing more effectively than it does particle concentration.

Table 2 displays the skin friction coefficient $\mathrm{Cf}_x\sqrt{\mathrm{Re}_x}$, Nusselt number $\mathrm{Nu}_x\mathrm{Re}_x^{\frac{-1}{2}}$, and Sherwood number $\mathrm{Sh}_x\mathrm{Re}_x^{\frac{-1}{2}}$ values as a function of the governing parameter alteration. These values are important because they help with the study and optimization of different engineering processes by offering vital insights into the system's mass and heat transport characteristics. Higher values of the magnetic parameter are found to be associated with a more significant fall in both the dimensionless Sherwood number and the dimensionless Nusselt number; for values of the skin friction coefficient, this pattern is inverted. While the local Nusselt number exhibits an opposite pattern with regard to the same parameter, the dimensionless skin friction coefficient and mass transfer rate decrease as the Casson parameter increases. Moreover, when the temperature ratio

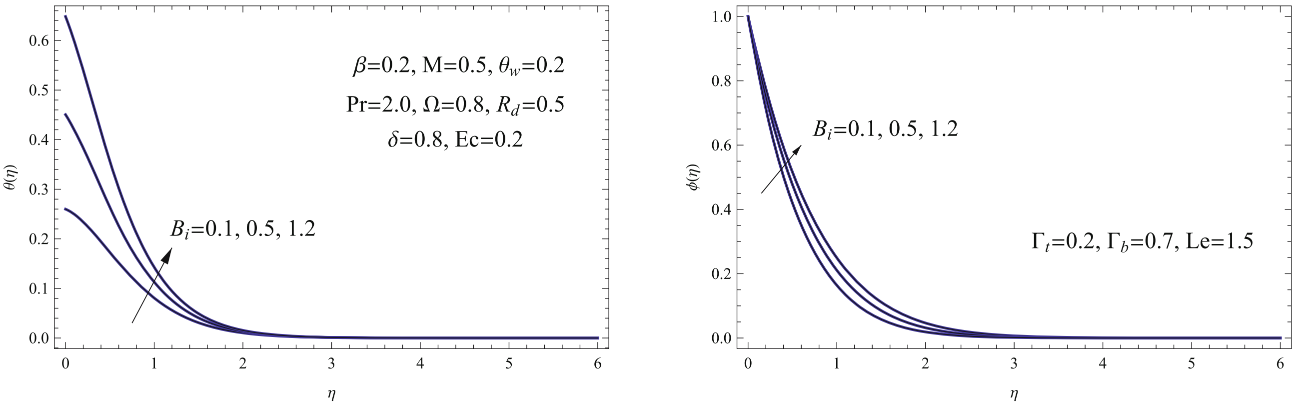

(a) (b)

Figure 5: (a) $\theta(\eta)$ for various B_i and (b) $\phi(\eta)$ for various B_i.

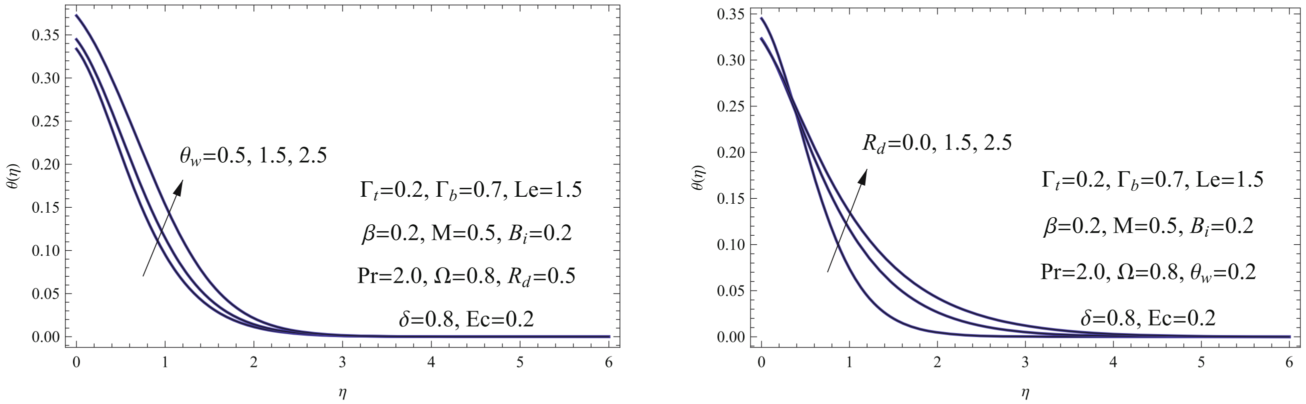

(a) (b)

Figure 6: (a) $\theta(\eta)$ for various θ_w and (b) $\theta(\eta)$ for various R_d.

parameter reaches significant magnitudes, there is a notable rise in both the dimensionless heat and mass transfer rates. Conversely, the opposite trend is observed for the thermophoresis parameter under similar conditions. Furthermore, it is worth noting that both thermal radiation and the Biot number possess the characteristic of augmenting the rate of heat transfer while simultaneously reducing the rate of mass transfer. The analysis of the tabular results reveals that both the temperature ratio parameter and Biot number demonstrate substantial influence on thermal transport characteristics. A key finding shows that incremental changes in either parameter produce a marked increase in the local Nusselt number, reflecting intensified thermal gradients at the boundary surface. These results underscore their pivotal function in governing thermal boundary layer development and system-wide heat transfer performance. Finally, this study's findings hold direct significance for maritime thermal systems. The improved heat transfer from higher Biot numbers and nanoparticle effects can optimize compact heat exchangers in marine energy systems. Additionally, the magnetic field's flow-damping behavior informs cooling strategies for ship engines utilizing magnetic flow control. These results establish a foundation for designing efficient nanofluid cooling solutions in marine applications.

6 Concluding remarks

This article utilizes the shooting method to effectively obtain precise solutions for the flow of Casson nanofluid near a stagnation point over a permeable stretching surface, taking into account both viscous dissipation and thermal radiation effects. The nanofluid model employed in this study incorporates the influences of magnetic fields,

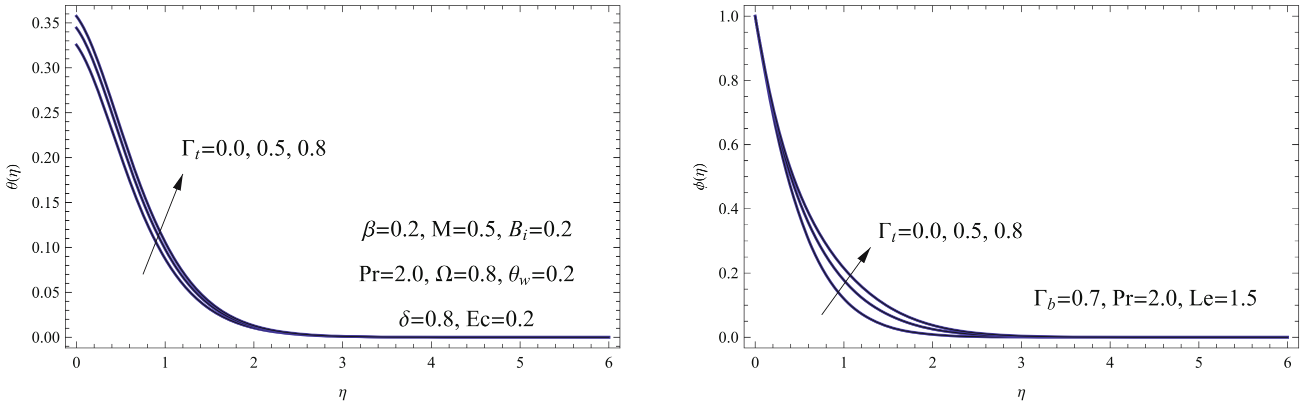

(a) (b)

Figure 7: (a) $\theta(\eta)$ for various Γ_t and (b) $\phi(\eta)$ for various Γ_t.

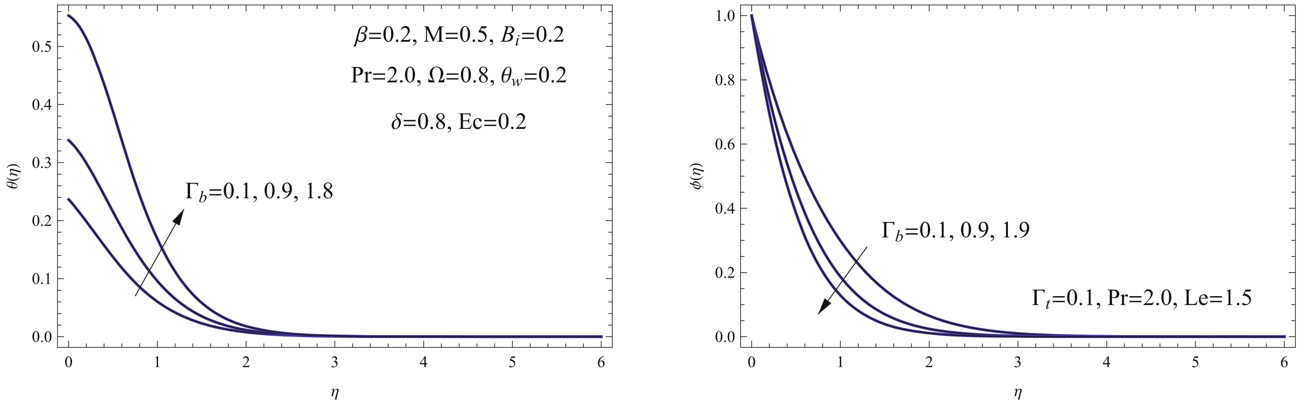

(a) (b)

Figure 8: (a) $\theta(\eta)$ for various Γ_b and (b) $\phi(\eta)$ for various Γ_b.

Brownian motion, Ohmic heating, and thermophoresis. In the present study, the nonlinear Rosseland approximation is utilized for thermal radiation modeling. The results obtained from this study are compared with those of prior research, revealing a remarkable agreement. The present analysis adopts a steady, two-dimensional framework with constant fluid properties, thereby excluding transient behavior and 3D effects, a recognized limitation of this study. The key findings of the numerical analysis are outlined as follows:

1) Clear linear reduction for the local Nusselt and Sherwood numbers is noted based on the magnetic parameter and thermophoresis parameter.
2) In contrast to the local Nusselt number, which rises with an increase in the Casson parameter, the local Sherwood number falls.

Table 2: $Cf_x\sqrt{Re_x}$, $Nu_x Re_x^{\frac{-1}{2}}$, and $Sh_x Re_x^{\frac{-1}{2}}$ for different values of governing parameters with Ω = 0.8, Le = 1.5, Ec = 0.2, and Pr = 2.0

δ	M	β	B_i	θ_w	R_d	Γ_t	Γ_b	$Cf_x\sqrt{Re_x}$	$Nu_x Re_x^{\frac{-1}{2}}$	$Sh_x Re_x^{\frac{-1}{2}}$
0.5	0.5	0.2	0.2	0.2	0.5	0.2	0.7	2.22130	0.131886	1.73615
0.8	0.5	0.2	0.2	0.2	0.5	0.2	0.7	1.97504	0.134008	1.71836
10	0.5	0.2	0.2	0.2	0.5	0.2	0.7	1.50172	0.138225	1.66509
0.8	0.0	0.2	0.2	0.2	0.5	0.2	0.7	1.74507	0.143619	1.72447
0.8	0.5	0.2	0.2	0.2	0.5	0.2	0.7	1.97504	0.134008	1.71836
0.8	2.0	0.2	0.2	0.2	0.5	0.2	0.7	2.53001	0.108968	1.70628
0.8	0.5	0.2	0.2	0.2	0.5	0.2	0.7	1.97504	0.134008	1.71836
0.8	0.5	0.5	0.2	0.2	0.5	0.2	0.7	1.35869	0.154307	1.75170
0.8	0.5	1.2	0.2	0.2	0.5	0.2	0.7	−0.64095	0.166849	1.85036
0.8	0.5	1.5	0.2	0.2	0.5	0.2	0.7	−1.69382	0.17449	1.9059
0.8	0.5	0.2	0.1	0.2	0.5	0.2	0.7	1.97504	0.073115	1.73079
0.8	0.5	0.2	0.4	0.2	0.5	0.2	0.7	1.97504	0.230248	1.69859
0.8	0.5	0.2	1.0	0.2	0.5	0.2	0.7	1.97504	0.442790	1.65491
0.8	0.5	0.2	0.2	0.5	0.5	0.2	0.7	1.97504	0.141597	1.71823
0.8	0.5	0.2	0.2	1.5	0.5	0.2	0.7	1.97504	0.358156	1.73615
0.8	0.5	0.2	0.2	2.5	0.5	0.2	0.7	1.97504	1.106301	1.76981
0.8	0.5	0.2	0.2	0.2	0.0	0.2	0.7	1.97504	0.130993	1.72101
0.8	0.5	0.2	0.2	0.2	1.5	0.2	0.7	1.97504	0.136970	1.71558
0.8	0.5	0.2	0.2	0.2	2.5	0.2	0.7	1.97504	0.138211	1.71433
0.8	0.5	0.2	0.2	0.2	0.5	0.0	0.7	1.97504	0.135449	1.73371
0.8	0.5	0.2	0.2	0.2	0.5	0.5	0.7	1.97504	0.131652	1.69826
0.8	0.5	0.2	0.2	0.2	0.5	0.8	0.7	1.97504	0.129020	1.68218
0.8	0.5	0.2	0.2	0.2	0.5	0.1	0.1	1.97504	0.153001	1.64152
0.8	0.5	0.2	0.2	0.2	0.5	0.1	0.8	1.97504	0.130698	1.72784
0.8	0.5	0.2	0.2	0.2	0.5	0.1	1.5	1.97504	0.089729	1.73591

3) Elevating the Biot number, magnetic number, and thermal radiation parameter, while lowering the Casson parameter, results in elevated temperature profiles.
4) Additionally, an escalation in both the Brownian motion parameter and the thermophoresis parameter causes higher temperatures within the boundary layer.
5) The rise in dimensionless concentration follows a consistent pattern for higher thermophoresis parameters, whereas the opposite trend occurs for the Brownian motion parameter.
6) Future work may consider unsteady effects, variable thermal conductivity, or variable thermal density to further enrich the analysis.

Acknowledgments: This work was funded by the Deanship of Graduate Studies and Scientific Research at Jouf University under grant No. (DGSSR-2024-02-02234).

Funding information: This research was supported by the Deanship of Graduate Studies and Scientific Research at Jouf University under grant No. DGSSR-2024-02-02234.

Author contributions: Essam Awwad conducted the investigation, developed the methodology and conceptual framework, formal analysis, validation, preparing the original draft, visualization and managed resources. Ahmed M. Megahed contributed to validation, drafting the original text, and visualization. Both authors reviewed the manuscript. All authors have accepted responsibility for the entire content of this manuscript and approved its submission.

Conflict of interest: The authors state no conflict of interest.

Data availability statement: All data generated or analysed during this study are included in this published article.

References

[1] Choi SUS. Enhancing thermal conductivity of fluid with nanoparticles, developments and applications of non-Newtonian flow. ASME FED. 1995;231:99–105.

[2] Ahmadi H, Rashidi A, Nouralishahi A, Mohtasebi SS. Preparation and thermal properties of oil-based nanofluid from multi-walled carbon nanotubes and engine oil as nano-lubricant. Int Commun Heat Mass Transf. 2013;46:142–7.

[3] Ijam A, Saidur R. Nanofluid as a coolant for electronic devices (cooling ofelectronic devices). Appl Therm Eng. 2012;32:76–82.

[4] Buongiorno J, Hu L-W, Kim SJ, Hannink R, Truong BAO, Forrest E. Nanofluids for enhanced economics and safety of nuclear reactors: an evaluation of thepotential features, issues, and research gaps. Nucl Technol. 2008;162:80–91.

[5] Alsabery AI, Chamkha AJ, Saleh H, Hashim I, Chanane B. Effects of finite wall thickness and sinusoidal heating on convection in nanofluid-saturated local thermal non-equilibrium porous cavity. Phys A Stat Mech Appl. 2017;470:20–38.

[6] Eastman JA, Choi SUS, Li S, Yu W, Tompson LJ. Anomalously increased effective thermal conductivities of ethylene glycol-based nanofluids containing copper nanoparticles. Appl Phys Lett. 2001;78:718–20.

[7] Harada N, Tsunoda K. Study of a disk MHD generator for nonequilibrium plasma generator (NPG) system. Energy Convers Manag. 1998;39:493–503.

[8] Shang JS. Recent research in magneto-aerodynamics. Prog Aero Sci. 2001;37:1–20.

[9] Abricka M, Krumins J, Gelfgat Y. Numerical simulation of MHD rotator action on hydrodynamics and heat transport in single crystal growth processes. J Cryst Growth. 1997;180:388–400.

[10] Subhas Abel M, Nandeppanavar MM. Effects of thermal radiation and non-uniform heat source on MHD flow of viscoelastic fluid and heat transfer over a stretching sheet. Int J Appl Mech Eng. 2007;12:903–18.

[11] Moghimi MA, Talebizadeh P, Mehrabian MA. Heat generation/absorption effects on magnetohydrodynamic natural convection flow over a sphere in a non-Darcian porous medium. Proc IME E J Process. Mech. Eng. 2011;225:29–39.

[12] Nandeppanavar MM, Subhas Abel M, Kemparaju MC. Stagnation point flow heat and mass transfer of MHD nanofluid due to porous stretching sheet through porous media with effect of thermal radiation. J Nanofluids. 2017;6:38–47.

[13] Khan M, Rasheed A, Anwar MS, Shah STH. Application of fractional derivatives in a Darcy medium natural convection flow of MHD nanofluid. Ain Shams Eng J. 2023;14:102093.

[14] Khan M, Zhang Z, Lu D. Numerical simulations and modeling of MHD boundary layer flow and heat transfer dynamics in Darcy-forchheimer media with distributed fractional-order derivatives. Case Stud Thermal Eng. 2023;49:103234.

[15] Khan M, Alhowaity A, Imran M, Hussien M, Alroobaea R, Anwar MS. Advanced numerical simulation techniques in MHD fluid flow analysis using distributed fractional order derivatives and Cattaneo heat flux model. ZAMM. 2024;104:e202300622.

[16] Khan M, Anwar MS, Imran M, Rasheed A. Nanofluid heat transfer in irregular 3D surfaces under magnetohydrodynamics and multi-slip effects. Front Heat Mass Transfer. 2024;22:1399–419.

[17] Ganesh GR, Sridhar W. MHD radiative Casson-Nanofluid stream above a nonlinear extending surface including chemical reaction through Darcy-Forchiemer medium. Heat Transfer 2021;50:7691–711.

[18] Singh J, Vishalakshi AB, Mahabaleshwar US, Bognar G. MHD Casson fluid flow with Navier's and second order slip due to a perforated stretching or shrinking sheet. Plos One. 2022;17:e0276870.

[19] Jaffrullah S, Sridhar W, Ganesh GR. MHD radiative casson fluid flow through Forchheimer permeable medium with joule heating influence. CFD Letters. 2023;15:179–99.

[20] Awati VB, Goravar A, Kumar NM, Bognár G. Stability analysis of magnetohydrodynamic Casson fluid flow and heat transfer past an exponentially shrinking surface by spectral approach. Case Stud Thermal Eng. 2024;60:104810.

[21] Lone SA, Anwar S, Saeed A, Bognár G. A stratified flow of a non-Newtonian Casson fluid comprising microorganisms on a stretching sheet with activation energy. Sci Reports. 2023;13:11240.

[22] Rani S, Reddy VR, Sridhar W, Akgül A, Alsharari MA, Asad J. MHD stagnation point radiative flow of hybrid Casson nanofluid across a stretching surface. Contemp Math. 2024;5:1590–605.

[23] Jaffrullah S, Sridhar W, Ganesh GR. Analysis of MHD casson nanofluid flow over a nonlinearly stretching surface with Joule heating, radiation and suction effects. Int J Heat Tech. 2024;42:414–26.

[24] Nihaal KM, Mahabaleshwar US, Joo SW, Bognár G. Bioconvection and chemical reaction impacts on Casson nanofluid flow on a thin needle: A stochastic approach. Therm Adv. 2025;3:100042.

[25] Alali E, Megahed AM. MHD dissipative Casson nanofluid liquid film flow due to an unsteady stretching sheet with radiation influence and slip velocity phenomenon. Nanotech Rev. 2022;11:463–72.

[26] Ghoneim NI, Megahed AM. Hydromagnetic nanofluid film flow over a stretching sheet with prescribed heat flux and viscous dissipation. Fluid Dyn Material Proces. 2022;18:1373–88.

[27] Amer AM, Al Rashdi SA, Ghoneim NI, Megahed AM. Tangent hyperbolic nanofluid flowing over a stretching sheet through a porous medium with the inclusion of magnetohydrodynamic and slip impact. Results Eng. 2023;19:101370.

[28] Mushtaq A, Mustafa M, Hayat T, Alsaedi A. Nonlinear radiative heat transfer in the flow of nanofluid due to solar energy: a numerical study. J Taiwan Inst Chem Eng. 2014;45:1176–83.

[29] Raptis A. Radiation and free convection flow through a porous medium. Int Commun Heat Mass Tran. 1998;25:289–95.

[30] Brewster MQ. Thermal radiative transfer properties. New York: John Wiley and Sons; 1972.

[31] Sparrow EM, Cess RD. Radiation heat transfer. Washington: Hemisphere; 1978.

[32] Ghasemi SE, Hatami M. Solar radiation effects on MHD stagnation point flow and heat transfer of a nanofluid over a stretching sheet. Case Stud Thermal Eng. 2021;25:100898.